



Life-extending Control of Mechanical Structures: Experimental Verification of the Concept*

S. TANGIRALA,† M. HOLMES,† A. RAY† and M. CARPINO†

Optimal feedforward and robust feedback control provides structural durability and desired performance of operating machinery. Experimental results are presented to demonstrate life extension of a mechanical structure with no significant loss of dynamic performance.

Key Words—Robust control; sampled-data control; vibration control; optimization; fatigue and fracture.

Abstract—The concept of life-extending control is built upon the two disciplines of *Systems Science* and *Mechanics of Materials*, and its goal is to achieve an optimized trade-off between dynamic performance and structural durability of the plant under control. Experimental and simulation results reported in recent publications show that a life extending control system can substantially reduce the structural damage accumulated in critical components with no significant loss of plant performance. This enhancement of structural durability is accomplished via nonlinear optimization to generate a sequence of open-loop commands that maneuver the plant from a known initial state, along a prescribed trajectory, close to the final desired-state subject to constraints on the damage rate and accumulation in critical components. This paper presents a methodology for analytical development of a robust feedforward-feedback control policy for life extension and high performance of mechanical structures. The concept of life-extending control is experimentally verified in a laboratory testbed which is a two-degree-of-freedom (2DOF) mechanical system excited by a computer-controlled shaker table. Test results demonstrate that the fatigue life of test specimens can be substantially extended with no appreciable degradation in the dynamic performance of the mechanical system. © 1998 Elsevier Science Ltd. All rights reserved.

1. INTRODUCTION

A major objective in control of complex mechanical systems such as electric power plants, transportation systems, advanced aircraft, and spacecraft is to achieve the mission objectives with increased reliability, availability, component durability, and maintainability. Therefore, performance, cost of maintenance and operation, and service life should be taken into consideration during the design process. In view of high-performance requirements and availability of improved materials that may have

significantly different damage characteristics relative to conventional materials, the lack of appropriate knowledge about the properties of these materials will lead to either of the following: (i) less than achievable performance due to overly conservative design; or (ii) over straining of the mechanical structures leading to unexpected failures and drastic reduction in service life. From this perspective, Ray *et al.* (1994a-c) have proposed a methodology to achieve an optimized trade-off between the system performance and structural durability of the plant under control. This concept, referred to as life-extending control (also known as damage mitigating control), is built upon the two disciplines of *Systems Science* and *Mechanics of Materials* where the decision and control policies are synthesized based on state-variable model(s) of structural damage in conjunction with the plant dynamic model.

Life-extending control is most effective in enhancing the structural durability of a plant component when that component contains degrees of freedom which are not directly controlled by the plant inputs. An example is damage reduction in turbine blades during the upthrust transient motion of a rocket engine where the oxidant flow into a preburner is controlled to meet the engine performance requirements (Ray *et al.*, 1994b, c). Here the torque in the turbopump, which is dependent on preburner gas temperature and pressure as well as on the main thrust chamber pressure, is only indirectly affected by the oxidant flow. Since the turbine blade vibrations are not directly controlled, these blades are subjected to thermomechanical fatigue damage even during normal operation. In contrast to conventional control system synthesis which only involves optimization of the system performance, the goal here is to achieve the specified performance of the engine while extending its

*Received 21 November 1995; revised 4 October 1996; received in final form 14 May 1997. This paper has not been presented in any IFAC Conference. *Corresponding author* Dr. Asok Ray. Tel. 001 814 865 6377; Fax 001 814 863 4848; E-mail axr2@psu.edu.

†Mechanical Engineering Department, The Pennsylvania State University, University Park, PA 16802, U.S.A.

service life. Simulation experiments showed a substantial reduction in the accumulated damage for an insignificant degradation in the rocket engine performance.

Tangirala *et al.* (1995) have experimentally verified the life-extending control concept on a laboratory tested by synthesizing optimal feedforward control policies to achieve a trade-off between service life and performance. Test results demonstrate: (i) extended fatigue life by up to three and a half times without significant performance degradation; and (ii) close agreement between the analytical prediction of damage and experimental observations. This paper extends the work reported there to include a robust life-extending feedback controller that improves the performance of the dynamic system while simultaneously reducing the accumulated damage in the test specimen.

The major tasks in the synthesis of a life-extending control system are: (i) dynamic modeling of the mechanical system to be controlled; (ii) formulation of a damage model for each of the identified critical components; (iii) synthesis of an open-loop control policy to achieve structural durability and high performance by minimizing a cost functional that represents performance specifications subject to damage constraints; and (iv) synthesis of a robust feedback controller that mitigates damage while satisfying the performance specifications. The paper is organized in a similar manner.

2. DESCRIPTION OF THE LABORATORY TESTBED

A laboratory testbed has been constructed to experimentally verify the life-extending control concept and to establish its feasibility. The testbed consists of a simple two degree-of-freedom (DOF) mass-beam system excited by the vibratory motion of a shaker table as shown in Fig. 1. One DOF is

directly controlled by the shaker table whereas the other DOF is not controlled, but is observable *via* position measurements of the vibrating masses. The test specimen, subjected to fatigue, is representative of a plant component suffering mechanical damage. The construction of the testbed facilitates easy re-configuration into more complex multi-input–multi-output systems with additional degrees of freedom. The testbed is logically separated into two subsystems: (i) the plant subsystem consisting of the mechanical structure including the test specimen to be damaged, actuators, and sensors; and (ii) the control and communications subsystem consisting of computers, data acquisition and processing, and communications hardware.

Here, the intent is to simplify the experimental investigation and facility as much as possible without compromising the key characteristics of the fundamental problem of damage sensing so that the underlying phenomena of damage can be clearly observed and interpreted from unambiguous experimental results. It is recognized that the physics of fatigue damage at room temperature in laboratory air are, in most cases significantly different from those at elevated temperatures of the plant environment. Nevertheless, the research work reported in this paper is a crucial step toward achieving the final goal of realizing life extending systems in actual plant operating environments (e.g. power plants).

The plant subsystem

The discussion here focuses on the basic testbed configuration in Fig. 1 where the mechanical system consists of two discrete masses supported on cantilever beams. The second mass is connected to a shaker table which acts as the actuator for the system through a flexible pivot. The flexible pivot rigidly links the translating mass in the actuator to the mass on the beam in the direction of motion.

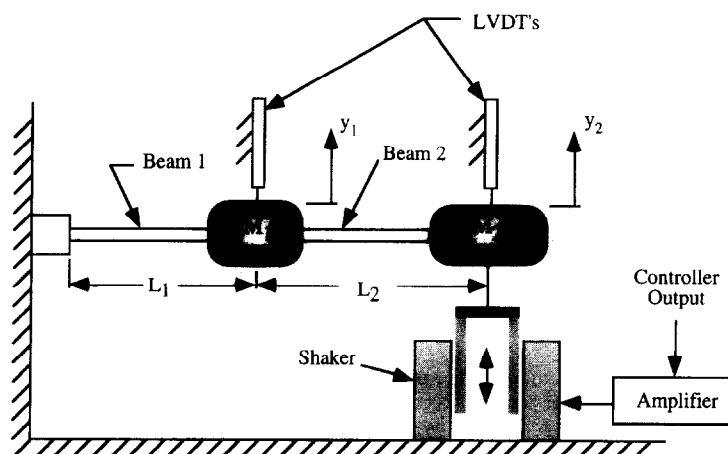


Fig. 1. Mechanical structure of the laboratory tested.

The translational positions of the masses are measured using linear variable differential transformer (LVDT) sensors which are located at the midpoints of the masses M_1 and M_2 . In the current configuration, the geometric parameters of the mechanical system are as follows:

Masses: $M_1 = 6.95 \text{ lb m}$ (3.153 kg); $M_2 = 2.70 \text{ lb m}$ (1.225 kg).

Beam 1: Material: Steel; Length $L_1 = 11.84 \text{ in}$ (301 mm); Height $H_1 = 0.437 \text{ in}$ (11.1 mm); Width $W_1 = 0.870 \text{ in}$ (22.1 mm); Young's modulus $E_1 = 30 \times 10^6 \text{ psi}$ ($2.068 \times 10^8 \text{ kN m}^{-2}$).

Beam 2: Material: 2024-T3 Aluminum alloy; Length $L_2 = 8.5 \text{ in}$ (216 mm);

Height $H_2 = 0.122 \text{ in}$ (3.1 mm); Width $W_2 = 0.437 \text{ in}$ (11.1 mm);

Young's modulus $E_2 = 10.5 \times 10^6 \text{ psi}$ ($7.24 \times 10^7 \text{ kN m}^{-2}$).

The failure site

Since the objective of this testbed is to investigate the influence of different control policies on specific modes of fatigue failure in a dynamic setting, a structurally weakened element which is representative of a critical plant component is introduced to ensure the occurrence of an observable failure. In the two mass configuration, two parallel failure sites are introduced by drilling a 0.312 in (7.92 mm) hole located 2.66 in (67.56 mm) from the center of mass M_1 as shown in Fig. 2. As the specimen is subjected to cyclic stresses, fatigue cracks initiate on the upper and lower surfaces of the beam and propagate through the thickness towards the neutral axis.

Modelling of the mechanical structure

A structural model of the mechanical system described above is formulated using a cubic interpolation polynomial to approximate the lateral (y -direction) displacement of the beams and a linear approximation for the lateral displacement of the masses. The major assumptions in the model formulation include:

- Lumped representation of the beam masses;
- Beam subjected to pure bending (i.e. negligible torsional effects);
- No deformation of the masses M_1 and M_2 .

The assumption that the masses, M_1 and M_2 , essentially behave as rigid bodies is justified by their relatively high stiffness. The actuator is assumed to force a point mass, M_2 , at the tip of beam 2 as seen in Fig. 1 whereas the mass M_1 is distributed in the longitudinal direction. The validity of the other assumption, i.e. negligible torsional effects is demonstrated by the close agreement between model predictions and experimental data.

Based on the above assumptions, lateral displacements of the beams 1 and 2, and the rigid distributed mass M_1 are represented as functions of the longitudinal distance, x , as

$$y_i(x) = C_{1i} \frac{x^3}{6} + C_{2i} \frac{x^2}{2} + C_{3i}x + C_{4i}$$

$$i = 1, 2 \text{ for the beams 1 and 2,} \quad (1)$$

$$y_3(x) = C_5x + C_6 \text{ for the mass } M_1.$$

The ten constants in equations (1) are evaluated by applying standard displacement, force, moment, and slope boundary and compatibility conditions (Crandall *et al.*, 1978) and using the physical dimensions listed above to yield the following dynamic equations of motion (details are given in Tangirala, 1996):

$$\begin{aligned} A_1 \ddot{y}_1 + B_1 \dot{y}_1 + C_1 y_2 &= 0, \\ A_2 \ddot{y}_2 + B_2 \dot{y}_1 + C_2 y_2 &= F, \end{aligned} \quad (2)$$

where $A_1 = 0.018$, $B_1 = 221.0$, $C_1 = -7.1541$, $A_2 = 0.007$, $B_2 = -7.1541$, $C_2 = 23.379$; \bar{y}_1 represents the lateral position of the center of mass, M_1 in inches, \bar{y}_2 represents the lateral position of the point mass, M_2 in inches; and F represents the force applied by the actuator to the point mass, M_2 . The positions \bar{y}_1 and \bar{y}_2 correspond to the locations of the position sensors on the experimental testbed.

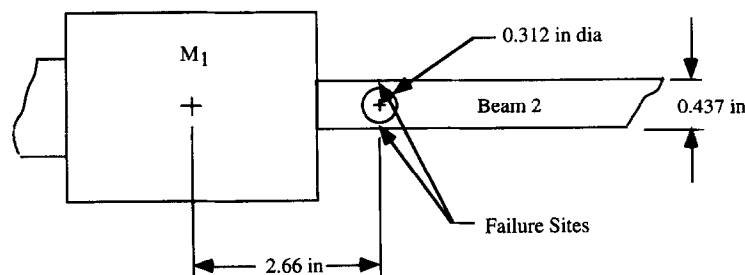


Fig. 2. Top view of the failure site on the beam specimen.

An eigenvalue analysis of this two-degree-of-freedom system indicates that the natural undamped frequencies of the first and second modes of vibration are 9.14 and 17.67 Hz, respectively. The stresses at the failure sites on beam 2 shown in Fig. 2 are given by (Crandall *et al.*, 1978)

$$\sigma_{FS} = -\bar{F} \frac{(L_2 - x_2)h}{I_{yy2}}, \quad (3)$$

where h is the distance from the neutral axis of beam 2, L_2 is the length of beam 2, x_2 is the distance of the center of the hole in beam 2 from mass M_1 , $\bar{F} = F - M_2\ddot{y}_2$ is the effective force (accounting for inertial effects) applied to mass M_2 , and I_{yy2} is the area moment of inertia of beam 2. Substituting for F from equation (2) and using physical dimensions, equation (3) is rewritten as

$$\sigma_{FS} = 1.99 \times 10^5 \bar{y}_1 - 9.4 \times 10^4 \bar{y}_2 \text{ psi} \quad (4)$$

at the top and bottom surfaces of beam 2 (i.e. at $h = H_2/2$). Equation (4) accounts for the increased local stress at the critical point due to the reduction in the area moment of inertia caused by the hole drilled in the specimen as seen in Fig. 2. The model in equations (2) represents the dynamics of the mass-beam system where the damping terms are assumed to be insignificant. The stresses computed via equation (4) show close agreement with experimentally measured stresses. The displacement sensors are modeled as pure gains (i.e. having negligible lag). The dynamics of the shaker table and the signal amplifier unit are mildly nonlinear and are influenced by the loading effects of the mass-beam system. The problem of determining the dynamic relationship between the applied voltage and the force generated in the actuator system was circumvented by using system identification techniques. Time-domain frequency-sweep excitation (Ljung, 1987) and experimentally measured data were used to identify a sixth-order voltage (actuator signal)-to-voltage (position sensors signal) transfer function. This data and the corresponding model outputs are shown in Fig. 3 and the resulting linear plant model is

$$\dot{\mathbf{x}} = \begin{bmatrix} -240.0 & 13.0 & 250.0 & -17.0 & 40.0 & -23.0 \\ 250.0 & -2.8 & 250.0 & 0.71 & -1.6 & 0.89 \\ -250.0 & -13.0 & 240.0 & 14.0 & -33.0 & 20.0 \\ -11.0 & 21.0 & -9.9 & -840.0 & 1200.0 & -370.0 \\ 1.0 & -1.6 & 0.56 & -210.0 & -97.0 & 300.0 \\ 6.7 & -14.0 & 7.6 & 170.0 & -820.0 & 650.0 \end{bmatrix} \mathbf{x} + \begin{bmatrix} -1.3 \\ -1.3 \\ -1.1 \\ -250.0 \\ 13.0 \\ 40.0 \end{bmatrix} u \quad (5)$$

$$\mathbf{y} = \begin{bmatrix} 1 & 0 & 0 & 0 & 0 & 0 \\ 0 & 0 & 0 & 1 & 0 & 0 \end{bmatrix} \mathbf{x} + \begin{bmatrix} 0 \\ 0 \end{bmatrix} u.$$

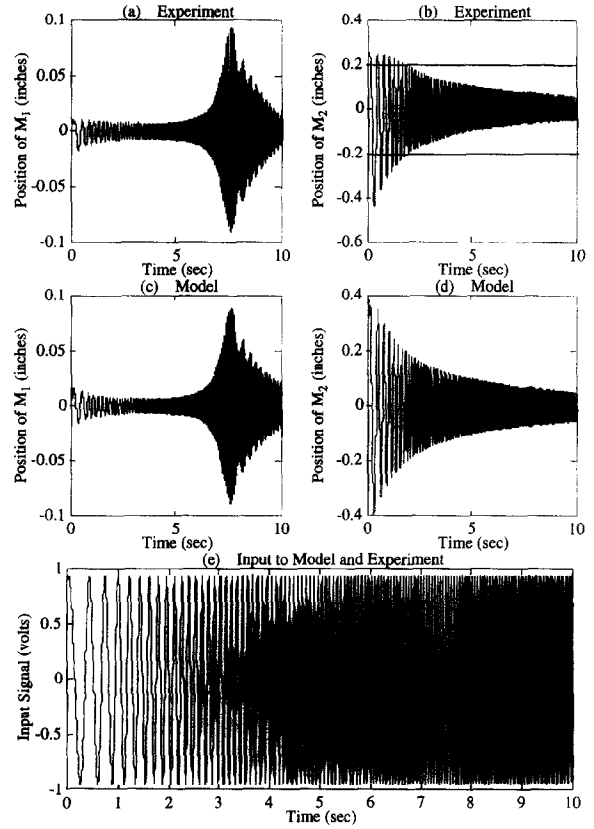


Fig. 3. Experimental and model response to frequency sweep input.

This experimentally identified model is used to represent the dynamics of the plant, and equation (4) models the time-dependent stress at the failure site.

Modeling of the fatigue damage process

Based on the work reported by Ray *et al.* (1994a), the fatigue damage model is formulated in the continuous-time setting. The model is first derived based on linear damage accumulation using a combination of Coffin-Manson and Basquin relationships (Bannantine *et al.*, 1990). Then, this linear damage model is modified following the damage curve approach (Bolotin, 1989) to account for dependence of the damage rate on the current state of

damage accumulation. Essential features of this fatigue damage model are presented in this section.

Converting the strain amplitudes into stress amplitudes from the cyclic stress–strain curve, the rates of both elastic damage δ_e and plastic damage δ_p (Suresh, 1991) are computed through differentiation as

$$\frac{d\delta_e}{dt} = \begin{cases} 2 \frac{d}{d\sigma} \left(\left(\frac{\sigma - \sigma_r}{2(\sigma_f - \sigma_m)} \right)^{-1/b} \right) \frac{d\sigma}{dt} & \text{for } \sigma > \sigma_r, \\ 0 & \text{otherwise,} \end{cases} \quad (6)$$

$$\frac{d\delta_p}{dt} = \begin{cases} 2 \frac{d}{d\sigma} \left(\frac{1}{\varepsilon_f'} \left(\frac{\sigma - \sigma_r}{2K'} \right)^{1/n'} \left(1 - \frac{\sigma_m}{\sigma_f'} \right)^{-c/b} \right)^{-1/c} \frac{d\sigma}{dt} & \text{for } \sigma > \sigma_r, \\ 0 & \text{otherwise,} \end{cases}$$

where the current stress σ and the stress rate $d\sigma/dt$ are obtained from the structural model; σ_r is the reference stress obtained using the rainflow method (Rychlik, 1993); $\sigma_m = (\sigma + \sigma_r)/2$ is the mean stress; and σ_f' , ε_f' , b , c , K' , n' are fatigue parameters under cyclic operations (Bannantine *et al.*, 1990; Boller and Seeger, 1987). Table 1 lists the fatigue parameters of 2024-T3 Aluminum alloy which is the material of the specimen used in this experimental study. The damage rate $d\delta/dt$ is obtained as the weighted average of the elastic and plastic damage rates such that

$$\frac{d\delta}{dt} = w \frac{d\delta_e}{dt} + (1 - w) \frac{d\delta_p}{dt}, \quad (7)$$

where the weighting function, w , is selected as the ratio of the elastic strain amplitude and total strain amplitude.

Equations (6) and (7) are then used to obtain the damage rate at any instant. Since mechanical structures are generally subjected to loads of varying amplitude, equation (6) which is based on the linear rule of damage accumulation will lead to erroneous results due to the sequence effect (Suresh, 1991).

Table 1. Fatigue parameters for 2024-T3 aluminum alloy

Strength coefficient, K'	81×10^3 psi (5.585×10^5 kN m ⁻²)
Strain hardening exponent, n'	0.039
Modulus of elasticity, E	10.5×10^6 psi (7.24×10^7 kN m ⁻²)
Fatigue strength exponent, σ_f'	114×10^3 psi (7.860×10^5 kN m ⁻²)
Fatigue ductility coefficient, ε_f'	0.197
Fatigue strength exponent, b	-0.082
Fatigue ductility exponent, c	-0.644

Therefore, the linear damage is modified *via* a nonlinear damage rule as follows:

$$D = (\delta)^{\gamma(\sigma, D)} \quad (8)$$

where D and δ are the current states of nonlinear and linear damage accumulation, respectively, and σ_a is the stress amplitude. $D \in (0, 1]$ describes the damage state for the duration of the component fatigue life. D is close to 0 for a virgin material and approaches 1 when failure is imminent. In any physical component, D is always greater than 0 because there is inevitably some initial damage due to material imperfections and machining marks. Equation (8) generates the following incremental change in damage accumulation and hence the damage rate:

$$\Delta D = \gamma(D^{\gamma-1}) \Delta \delta + \left(\frac{D(\ln D)}{\gamma} \right) \Delta \gamma \quad \text{and} \quad (9)$$

$$\dot{D}(t) \approx \frac{\Delta D(t)}{\Delta t}.$$

It follows from a crack propagation model such as the Pairs model (Paris and Erdogan, 1963) that the crack growth rate is dependent not only on the stress amplitude but also on the current crack length. Since the characteristics of γ in equation (9) may strongly depend on the type of the material, availability of pertinent experimental data for the correct material is essential for life-extending control. An approach to evaluate γ at selected discrete levels of stress amplitude by interpolation based on the experimental data is given in Ray *et al.* (1994a).

3. OPEN-LOOP CONTROL SYNTHESIS

The open-loop control policy is generated via nonlinear programming which consists of optimizing a cost functional subject to specified constraints (Tangirala *et al.*, 1995; Tangirala, 1996). These constraints are both physically motivated, such as actuator limits, and based on damage rate and accumulation in the critical components. For the optimization, the inputs are applied to the plant model described above; the outputs of the plant model are used by the structural model in equation (4) to determine the local stresses experienced by the material at the failure site on beam 2. These stresses and the corresponding stress rates are inputs to the damage model in equations (6)–(9) which computes the instantaneous accumulation and rate of fatigue damage developed at the failure site in Fig. 2. The configuration for generation of optimum feedforward input sequence is shown in Fig. 4. If the plant model is completely controllable, then there exists a control sequence that can maneuver the plant

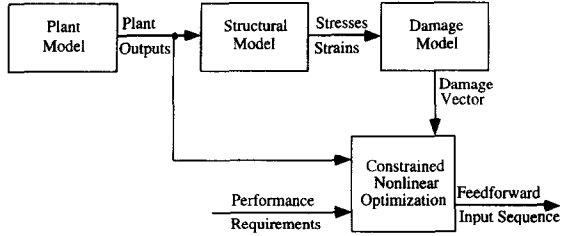


Fig. 4. Generation of optimal feedforward input sequence via nonlinear optimization.

from any arbitrary initial state to any specified final state. However, this does not guarantee that a solution exists for every constrained optimization problem. Whenever the admissible control inputs are restricted to a feasible set, certain final states may not be accessible without violating some of the constraints. In this work, a general purpose of nonlinear programming software package NPSOL (Gill *et al.*, 1991) has been used to solve the open-loop constrained optimization problem. The details are reported by Ray *et al.* (1994b, c).

Cost functional and constraints

The nonlinear optimization is realized *via* minimization of a cost functional, which includes performance specifications, subject to physical and damage constraints. The optimization yields an optimal control sequence, $\{\mathbf{u}_k\}$, that maneuvers the plant from a known initial condition to a specified final state, without violating any of the constraints. The quadratic cost functional is chosen to be the weighted ℓ_2 norm of the error in selected plant outputs and the control inputs. The cost functional is of the form

$$J(\mathbf{u}_k) = \sum_{k=0}^{N-1} ([\mathbf{y}_{k+1} - \mathbf{y}_{k+1}^{\text{nom}}]^T \mathbf{Q}_k [\mathbf{y}_{k+1} - \mathbf{y}_{k+1}^{\text{nom}}] + [\mathbf{u}_k - \mathbf{u}_k^{\text{nom}}]^T \mathbf{R}_k [\mathbf{u}_k - \mathbf{u}_k^{\text{nom}}]), \quad (10)$$

where N is the total number of discretized steps which represent the period from the initial time t_0 to the final time t_f of the maneuver; $\{\mathbf{y}_k^{\text{nom}}\}$ is the desired nominal trajectory of the regulated output \mathbf{y} ; $\{\mathbf{u}_k^{\text{nom}}\}$ is the input sequence that results in the best possible performance without taking damage into consideration; the penalty matrices, \mathbf{Q}_k and \mathbf{R}_k are symmetric positive definite with compatible dimensions. The minimization is carried out subject to constraints. Constraints on the control input sequence, $\{\mathbf{u}_k\}$, represent actuator saturation and hard limits on the actuator stroke. Additionally, pre-assigned limits are imposed on the damage rate at each sample instant to ensure structural durability. These conditions take the following form:

Natural bounds: $-\alpha \leq \mathbf{u}_k \leq \alpha$ for

$$k = 1, \dots, N-1, \quad (11)$$

Damage rate constraints: $\dot{\mathbf{D}}_k \leq \beta_k$ for

$$k = 1, \dots, N, \quad (12)$$

where α is the actuator limit, β_k is the specified tolerance for damage rate and $\mathbf{D}_k = \mathbf{D}(t)|_{t=t_k}$. Constraints are not applied to the accumulated damage \mathbf{D}_k since the actual damage accrued in any given cycle is very small (leading to precision problems) and varies nonlinearly with specimen fatigue. Reducing the damage rate in a cycle of operation results in the reduction of the damage accumulated during that cycle, leading to an increase in the service life of the system. Due to the optimization, this increase in life can be achieved with only a marginal loss of performance. The weight on the control inputs is included to avoid large fluctuations of the input signal as this could lead to chatter and damage in the actuator. The relative weights on the two parts of the cost functional and the damage rate constraint function are selected by the design engineer to emphasize performance, transient plant behavior, damage dynamics or control effort as required. It should be noted, however, that increasing the damage rate constraint has a direct impact on the system performance. So, a judicious selection of the constraints and weights can result in, within limits, different levels of damage mitigation with an associated loss of performance.

Problem formation

The problem is to generate, for the mass-beam structure shown in Fig. 1, an optimal control law that will make a trade-off between the conflicting requirements of performance and damage mitigation over the time interval $[t_0, t_f]$. This optimization problem is represented in the discrete-time setting to find an optimal control sequence $\{\mathbf{u}_k\}$ that will maneuver the plant from a known initial condition to a prescribed final state subject to:

- The dynamic system in equations (5);
- The actuator limits in equation (11); and
- The constraints on the damage rate in equation (12).

In the mechanical system of Fig. 1, the voltage input to the shaker table directly controls the position of the mass M_2 . The frequency of operation of the shaker table is 5.81 Hz (i.e. a full cycle period of 172 ms), which is one-third of the second natural frequency of the testbed, 17.45 Hz (which is slightly different from that predicted by the model). Note that the third harmonic of this frequency excites

mass M_1 , which is not directly controlled by the shaker table, to resonance. The optimization is carried out over one half-cycle of motion with the displacement of M_2 chosen as the regulated output. The nominal output profile is determined by the closest approximation to a half-square wave that the displacement trajectory of M_2 can achieve on the actual dynamic system over one-half cycle of operation. The input sequence that generates this nominal output profile constitutes the unconstrained (nominal) input to the system. Resonance of M_1 causes fatigue damage at the failure site on the test specimen shown in Fig. 2. This is a direct consequence of the high local stresses at the failure site caused by the large displacement of M_1 relative to M_2 . This configuration is, therefore, representative of a real physical situation where the specification of performance requirements in one subsystem of a dynamic system may lead to fatigue damage in other subsystems.

The sampling rate is selected as 4.3 ms, which is achievable on the Pentium-based control computer of the experimental facility. The sampling rate results in a total of 20 discrete time steps to maneuver the mass M_2 from an initial position of -0.2 in (5.08 mm) to a final position of $+0.2$ in (+5.08 mm) over one half of the period of vibration. Simulation results show that the maximum damage rate experienced at the failure site due to this maneuver is approximately $27 \times 10^{-6} \text{ s}^{-1}$ based on an assumed initial damage of 0.005. Three damage rate constraints of 5.0×10^{-7} , 1.0×10^{-7} and 0.5×10^{-7} are therefore chosen for the optimization task. It should be noted, however, that the initial damage of the specimen is a random variable (Ray and Tangirala, 1996) which depends on several factors like the machining quality, the heat treatment, size of the the notch, etc. The level of initial damage used in the optimization has a significant effect on the damage rate and accumulation due to nonlinearities in the damage dynamics. Further, the γ -parameters in equations (8) and (9) at different levels of damage need to be obtained for various stress amplitudes based on experimental fatigue crack growth data and linear damage prediction data generated by equations (6) and (7). Since experimental data for short crack growth of 2024-T3 aluminum is not available, the γ -parameters in the nonlinear damage model for 2024-T3 aluminum are evaluated in the appropriate stress range after adjusting those for 4340 steel that were reported by Ray *et al.* (1994a). Although the predicted damage may not be accurate in the absolute sense due to possibly inexact γ -parameters and incorrect initial conditions, the profile of damage dynamics generated by this model shows the right trend. Therefore, this damage information is considered to be sufficient for comparison

of the results of unconstrained and constrained optimization.

Remark. Stress at the failure site [equation (4)] and hence, the accumulated damage and damage rates [equations (8) and (9)] are functions of the two plant outputs \bar{y}_1 and \bar{y}_2 . Therefore, the stresses (or equivalently, a function of \bar{y}_1 and \bar{y}_2) can be used as constraints in the optimization instead of the damage; however, if the stresses are used, two constraints, either maximum stress and stress ratio, or maximum and minimum stress need to be specified.

4. FEEDBACK CONTROLLER SYNTHESIS

This section presents the synthesis of the sampled-data feedback control system (Bamieh and Pearson, 1992) based on a continuous-time plant model. The main objective of the feedback portion of the feedforward/feedback control law is to compensate for modelling uncertainties and additional disturbances and thereby enhance robust stability and performance of the dynamic system. The goal of the feedback control synthesis procedure is to achieve this objective without sacrificing the fatigue life of the test specimen which is a representation of a critical plant component. The linear feedback controller should minimize the tracking error of the position of mass M_2 in Fig. 1 without increasing the resonant vibration of mass M_1 . This is accomplished by appropriate selection of the (frequency-dependent) weighting functions used for synthesis of the feedback control law. This section presents the synthesis of two controllers: (i) a life-extending controller that considers damage and performance; and (ii) a non-life-extending controller that considers performance alone, i.e. a pure performance controller.

The setup used for feedback controller synthesis is shown in Fig. 5. The linear model used for this purpose is the one that is obtained via system identification in equation (5). The only plant output of interest here is the position, \bar{y}_2 , of the center of the mass M_2 . The performance objective is to have

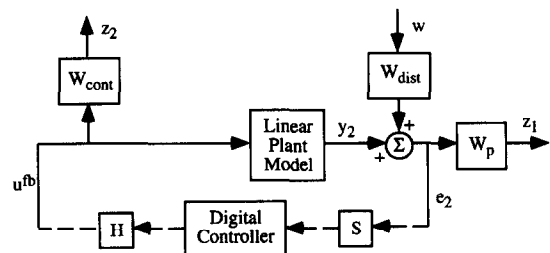


Fig. 5. Controller synthesis block diagram.

\bar{y}_2 follow a tracking signal which, in this case, is chosen to be the sequence $\{y_u^{ff}\}$ of unconstrained outputs. The rationale for choosing the unconstrained output sequence as the tracking signal with the constrained input sequence as the feedforward control signal is to increase system performance relative to that resulting from the constrained input. If this performance enhancement can be achieved with a controller that restricts the magnitude of the third harmonic component in the feedback signal, then there will be no significant change in the service life relative to the open-loop constrained case. The magnitude plot of the Fourier transform of $\{y_u^{ff}\}$ peaks at a frequency of 5.8 Hz and abruptly rolls-off thereafter. Therefore, to model the frequency contents of $\{y_u^{ff}\}$, the (frequency-dependent) disturbance weighting function (Packard *et al.*, 1993) is chosen to be

$$W_{dist}(s) = \frac{100}{s + 100} \quad (13)$$

which has a low-frequency gain of 1, and a break frequency of 100 rad s^{-1} which is larger than the peak frequency of $\{y_u^{ff}\}$, 5.8 Hz (36.44 rad s^{-1}). To satisfy the performance requirements, the error signal, $\bar{y}_2 - y_u^{ff}$, is scaled by the performance weight $W_p(s)$ during the controller synthesis. For the design of the life-extending controller, a performance weight $W_p(s)$ that is constant at all frequencies with a gain of 12 is found to yield the best results;

however, for the non-life-extending controller,

$$W_p(s) = \frac{2400}{s + 300} \quad (14)$$

results in acceptable performance.

The weight on the control effort, $W_{cont}(s)$, serves a dual purpose. For the non-life extending controller synthesis, it is used to prevent actuator saturation by penalizing the feedback signal at all frequencies. For the life-extending controller, $W_{cont}(s)$ is also used to mitigate damage by penalizing the feedback signal at harmful frequencies. In general, for a complex mechanical system, harmful frequencies are identified via a spectral analysis of the constrained and unconstrained input sequences obtained from the open-loop control policy synthesis described above. In this experimental testbed, the fast Fourier transform (FFT) responses of the unconstrained and constrained feedforward input sequences in Fig. 14 clearly demonstrate the fact that the third harmonic is the harmful frequency. To prevent the feedback signal from having large magnitudes at the resonance frequency, $W_{cont}(s)$ should have a large gain at the frequency 17.4 Hz ($109.33 \text{ rad s}^{-1}$). Figure 6 exhibits the magnitude plots of $W_{cont}(s)$ as well as the other weights used in the analysis and synthesis for the life extending controller and the non-life-extending controller.

The design goal here is to find a stabilizing discrete-time controller such that the induced L_2 -norm of the transfer matrix from w to $[z_1 \ z_2]^T$ is

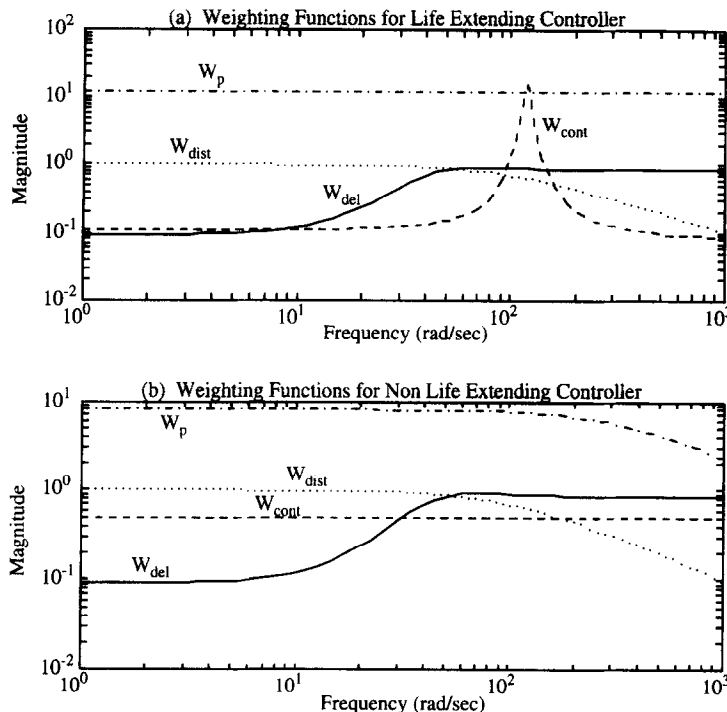


Fig. 6. Controller synthesis and analysis weighting functions.

minimized. Recently, several publications have appeared in the control literature which address the problem of optimal L_2 -induced controller synthesis. Bamieh and Pearson (1992) proposed a solution to the problem of optimal L_2 -induced norm synthesis for sampled-data systems, which has, subsequently, been incorporated into the function *sdhfsyn* in the MATLAB μ -Analysis and Synthesis toolbox. This approach makes use of a lifting technique which takes intersample behavior into account in the controller synthesis procedure. The sampled-data problem is recast in terms of an equivalent discrete-time H_∞ synthesis problem. Since there exists no isometric isomorphism between the time-domain ℓ_2 -space and the frequency-domain H_∞ -space, the combination of time domain and frequency-domain optimization allows ample flexibility in making the trade-off between dynamic performance and structural durability.

The non-life-extending controller is comprised of 10 states, while the life-extending controller has 13 states because additional states are necessary to realize the control input weighting function. Figure 8 shows the frequency responses of the transfer functions from u^{ff} to u^{fb} , $PK/(1 - PK)$, and from y^{ref} to u^{fb} , $K/(1 - PK)$, of the closed-loop system in Fig. 7 with the life-extending controller. Each of these transfer functions has a notch at $\sim 110 \text{ rad s}^{-1}$ which is responsible for damage mitigation. Note that although u^{ff} is not included in the feedback controller synthesis, the transfer function $PK/(1 - PK)$ contains a notch at $\sim 110 \text{ rad s}^{-1}$ because of the notch in $K/(1 - PK)$. Figure 9 shows the configuration used for the analysis of stability robustness. The dynamics contained within the dotted box represents a set of plants, \mathbf{P} , parametrized by $\Delta(s)$, which represents any stable transfer function that satisfies the bound $\|\Delta\|_\infty \leq 1$. It is assumed that the actual plant, P_{act} , is contained in \mathbf{P} , i.e. $P_{act} = (1 + W_{del}\Delta)P_{lin}$, for some $\|\Delta\|_\infty \leq 1$, where P_{lin} is the linear plant model. The selection of W_{del} is based on a comparison between the Bode plot of the linear model and a Bode plot created from experiments performed on the actual system. The magnitude of W_{del} at each frequency is chosen to be

$$|W_{del}(j\omega)| = \left| \frac{P_{act}(j\omega) - P_{lin}(j\omega)}{P_{lin}(j\omega)} \right|. \quad (14)$$

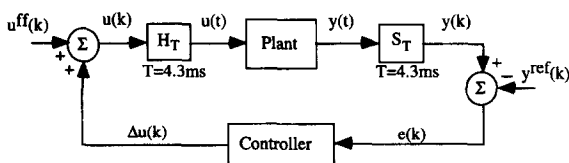


Fig. 7. Generalized closed-loop system.

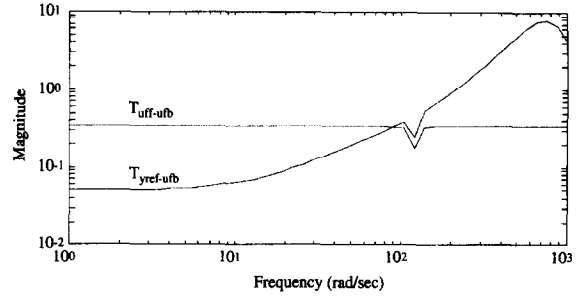


Fig. 8. Closed-loop system frequency response.

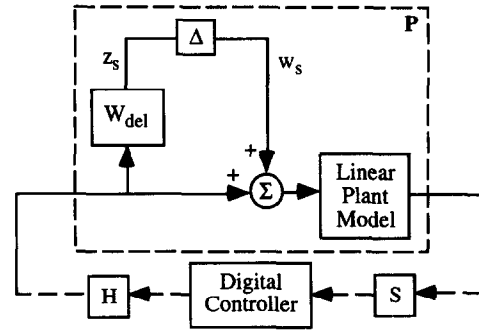


Fig. 9. Robust stability block diagram.

Using this data, a stable W_{del} can be created. Analysis of the robust stability of sampled data systems has been explored in a paper by Sivashankar and Khargonekar (1993). A sampled-data system is robustly stable if

$$\|T_{z_s, w_s}\|_{L_2\text{-ind}} < 1, \quad (15)$$

where T_{z_s, w_s} is the closed-loop input-output operator between w_s and z_s . The robust stability measures for the life-extending and nonextending controllers are 0.962 and 0.997, respectively.

5. EXPERIMENTAL RESULTS AND DISCUSSION

The constrained optimization yields an input sequence for each of the three damage rate constraints defined above. The corresponding output profiles of mass M_2 from simulation of the plant model are shown in Figs 10–12 (along with the unconstrained output) with increasing constraint level, respectively. The damage rates developed over one-half cycle for each of the three cases are shown in Fig. 13 where the effects of the constraints are clearly evident. Figure 10 shows that the loss of performance, as defined by the deviation from the unconstrained output profile, is quite small for a substantial decrease in the damage rate. Figures 11–13 clearly demonstrate the effects of increasing the damage constraint on the performance. This leads to the conclusion that based on the age and

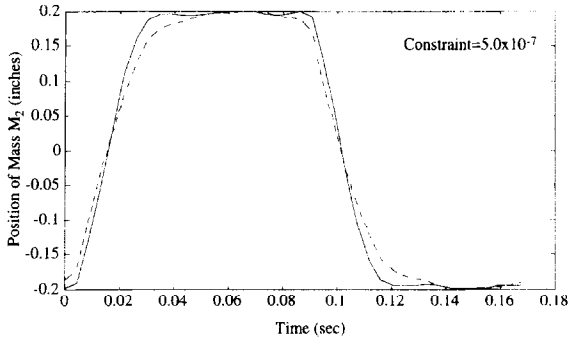


Fig. 10. Position of M_2 with open-loop constrained input (minimum constraint).

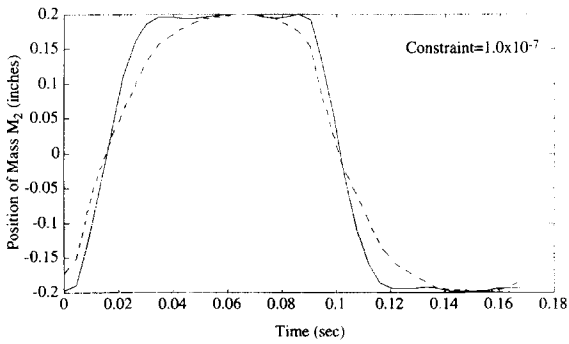


Fig. 11. Position of M_2 with open-loop constrained input (medium constraint).

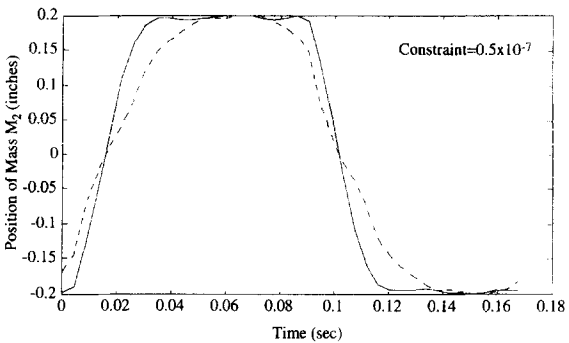


Fig. 12. Position of M_2 with open-loop constrained input (maximum constraint).

condition of a component, an appropriate input sequence can be chosen that will ensure safe performance albeit at a degraded level. Fig. 14(a)–(d) shows the fast Fourier transforms (FFT) of the constrained and unconstrained input sequences. The FFT of each of the constrained sequences shows a marked reduction in the magnitude of the third-harmonic component at ~ 17.5 Hz relative to the unconstrained waveform. As mentioned earlier, this third harmonic excites resonance of the mass, M_1 , and is the major factor causing fatigue damage at the failure site. Life extension of the mechanical structure by attenuation of the input

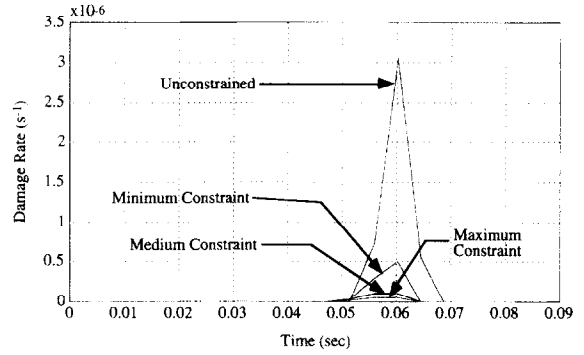


Fig. 13. Damage rates for unconstrained and constrained cases.

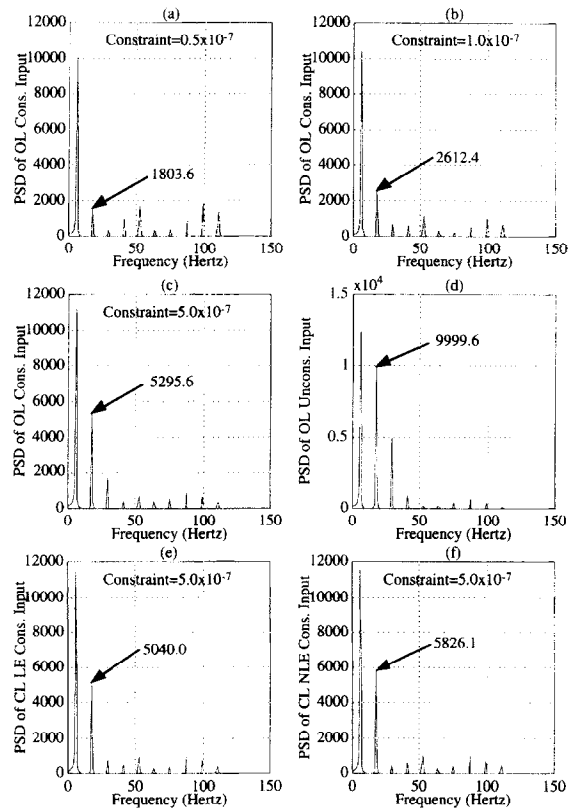


Fig. 14. FFTs of constrained and unconstrained inputs.

excitation, via a fixed-parameter band-stop filter for example is not a solution because the loss of dynamic performance may not be acceptable. Therefore, the magnitude of the third-harmonic component (which is the cause of damage in this case) is substantially reduced by optimization of the feedforward control policy while some of the other (apparently harmless) higher harmonics are moderately increased to minimize the loss of performance.

Figure 15 compares the performance of the experimental closed-loop system with the life-extending controller with the constrained (minimum constraint) and unconstrained open-loop performance. The improvement in performance is evident

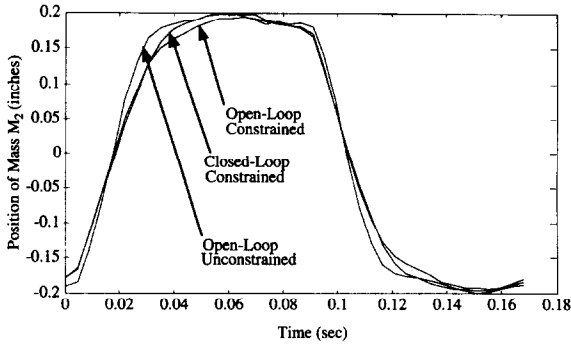


Fig. 15. Open-loop and closed-loop constrained outputs.

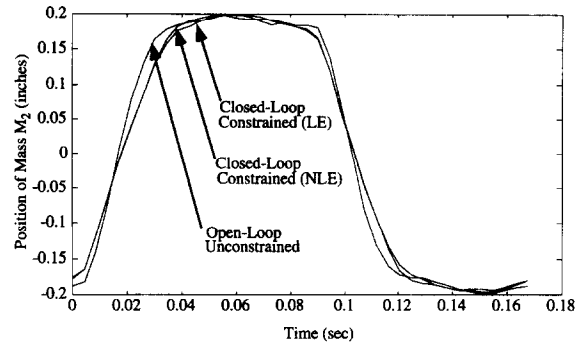


Fig. 16. Life-extending and non-life-extending controller outputs.

from the increased speed of response and the better “steady-state” performance. The resulting output trajectory of mass M_2 is closer to the reference signal and attains the prescribed final position faster. The FFT of the closed-loop input sequence, shown in Fig. 14(e), reveal that this enhanced performance is achieved with a reduction in the magnitude of the third-harmonic component in u relative to u^{ff} (Fig. 7), which causes less damage to the test specimen. The primary objective of the feedback controller design is to guarantee robust stability and enhance performance of the experimental test-bed with a small change in the accumulated damage. The third-harmonic content of u may be slightly increased or decreased depending on the relative magnitude and phase of the third-harmonic components of u^{ff} and u^{fb} . The FFTs of u^{ff} and u^{fb} for the closed-loop experiments show that the third-harmonic components have power spectral densities of 72.7706 and 12.0514, respectively. The phase difference between the third-harmonic components of u^{ff} and u^{fb} is 103.2126° . Elementary computations reveal that, for these signals, a phase difference in the range of $(94.75^\circ, 265.25^\circ)$ will result in a smaller third-harmonic component of u relative to that of u^{ff} . Therefore, in this particular case, a reduction in damage is achieved. However, this damage reduction via feedback compensation may not be achievable in general. Since the design of the controller can be considered as a frequency domain optimization problem, this result clearly demonstrates the usefulness of a mixed frequency and time-domain design approach. Figure 16 shows the performance of the closed-loop system with the non-life-extending controller. A moderate increase in performance relative to the life-extending controller is achieved. However, Fig. 14(f) shows that this performance enhancement is achieved at the cost of more damage accumulation as a result of the increase in the magnitude of the third-harmonic component in the input sequence.

Table 2 lists the mean time to failure for several experiments using the unconstrained and

Table 2. Summary of experimental results

Test condition	Average time of failure (s)	Measure of performance loss
Open-loop unconstrained	465	0.0
Open-loop constrained	1138	0.5172
Closed-loop constrained	1559	0.4647

constrained open-loop inputs and also the constrained input with the life-extending feedback controller. These experiments were conducted using identical specimens that were machined from the same stock of 2024-T3 Aluminum. The loss in performance is measured using the ℓ_1 -norm of the error signal which is the difference between the closed-loop trajectory of the position the mass M_2 and the desired trajectory (i.e. the output signal under the unconstrained feedforward control). Based on the ensemble of experimental data, the mean value of specimen life is found to be ~ 465 s for the unconstrained case, ~ 1338 s for the constrained case, and ~ 1559 s under feedforward–feedback control. These results show an increase in life by a factor of 2.88 between the unconstrained and constrained cases with a loss in performance of 0.5172, and an increase in life by a factor of 3.35 between the unconstrained and closed-loop cases with a loss in performance of 0.4647. The feedforward–feedback control yields stability robustness, improved performance, and longer fatigue life as compared to the feedforward control based on constrained optimization. The non-life-extending feedback controller results in a loss of performance of 0.4566 which is the best performance index using the constrained input.

6. SUMMARY AND CONCLUSIONS

This paper presents an extension and experimental verification of the work reported in a recent two-part paper (Ray *et al.*, 1994a, b) which

introduced the concept of life-extending control built upon the two disciplines of *Systems Science* and *Mechanics of Materials*. The theme of life extending control of mechanical systems can be summarized as follows:

Enhanced structural durability and high performance can be obtained if feedforward control commands are designed incorporating operational information and damage characteristics. Further improvement is possible utilizing a feedback controller that adds robustness and disturbance rejection while shaping the input command at the same time identifying and minimizing the magnitude of harmful components in the input commands. Following this approach, the functional life of critical components can be extended resulting in increased safety, reliability and availability and lower maintenance costs under diverse operating conditions.

A testbed has been constructed to experimentally verify the concept of robust life extending control of mechanical systems. The plant dynamics are modeled in the state-variable setting via system identification and a feedforward-feedback structure is selected for the control system. The feedforward control sequence is formulated based on the plant-dynamic model via constrained optimization of both performance and structural durability in the time domain. A robustly stable sampled-data feedback controller which is synthesized in the frequency domain is superimposed on the feedforward controller. This combination of time-domain and frequency-domain optimization allows ample flexibility in making the trade-off between dynamic performance and structural durability. The feedforward-feedback control yields stability robustness, improved performance, and longer fatigue life as compared to the feedforward control based on constrained optimization.

Experimental results demonstrate an increase in the life of test specimens by a factor of ~ 3.5 with little loss in performance. Experimental data shows evidence of random fatigue (Ray et al., 1995). This suggests restructuring the governing equations of damage dynamics in the stochastic setting, and formulating the control law via stochastic optimization.

The concept of life extending control of mechanical systems can be applied to a wide spectrum of engineering applications such as reusable rocket engines for space propulsion, rotating and fixed wing aircraft, fossil and nuclear plants for electric

power generation, automotive and truck engine/transmission systems, and large rolling mills. In each of these systems, damage-mitigating control can enhance safety and productivity accompanied by reduced life cycle cost.

Acknowledgements—The authors acknowledge benefits of discussion with Professor Mario Szaiaer of Penn State University. The work presented in this paper has been supported by National Science Foundation under Grant Nos. CMS-9531835 and DMI-9424587; National Science Foundation under research equipment Grant No. MSS-9112609; NASA Lewis Research Center under Grant Nos. NAG 3-1240 and NAG 3-1673.

REFERENCES

- Bamieh, B. A. and J. B. Pearson (1992). A general framework for linear periodic systems with applications to H_∞ sampled-data control. *IEEE Trans. Automat. Control*, **37**(4), 418–435.
- Bannantine, J. A., J. J. Comer and J. L. Handrock (1990). *Fundamentals of Metals Fatigue Analysis*. Prentice-Hall, Englewood Cliffs, NJ.
- Boller, C. and T. Seeger (1987). *Material Data for Cyclic Loading*. Elsevier, Amsterdam.
- Bolotin, V. V. (1989). *Prediction of Service Life for Machines and Structures*. ASME Press, New York.
- Crandall, S. H., N. C. Dahl and T. J. Lardner (1978). *An Introduction to the Mechanics of Solids*. McGraw-Hill, New York.
- Gill, P. E., W. Murry, M. A. Saunders and M. H. Wright (1991). *NPSOL Version 4.06*, Software Distribution Center, Stanford University, Palo Alto, CA.
- Ljung, L. (1987). *System Identification: Theory for the User*. Prentice-Hall, Englewood Cliffs, NJ.
- Packard, A., J. Doyle and G. Balas (1993). Linear, multivariable robust control with a m perspective. *J. Dyn. Systems Measurements Control Trans. ASME 50th Anniversary Issue*, **115**, 428–438.
- Paris, P. C. and F. Erdogan (1963). A critical analysis of crack propagation laws. *ASME J. Basic Engng*, **D85**, 528–534.
- Ray, A., M.-K. Wu, M. Carpino and C. F. Lorenzo (1994a). Damage-mitigating control of mechanical systems: Part I — Conceptual development and model formulation. *ASME J. Dyn. Systems Measurement Control*, **116**(3), 437–447.
- Ray, A., M.-K. Wu, M. Carpino and C. F. Lorenzo (1994b). Damage-mitigating control of mechanical systems: Part II — Formulation of an optimal policy and simulation. *ASME J. Dyn. Systems Measurement Control*, **116**(3), 448–455.
- Ray, A., X. Dai, M.-K. Wu, M. Carpino and C. F. Lorenzo (1994c). Damage-mitigating control of a reusable rocket engine. *AIAA J. Propulsion Power*, **10**(2), 225–234.
- Ray, A. and S. Tangirala (1996a). Stochastic modeling of fatigue crack dynamic for on-line fatigue prognostics. *IEEE Trans. Control Systems Technol.* **4**(2), 443–451.
- Rychlik, I. (1993). Note on cycle counts in irregular loads. *Fatigue Fracture Engng Mater. Struct.*, **16**(4), 377–390.
- Sivashankar, N. and P. P. Khargonekar (1993). Robust stability and performance analysis of sampled-data systems. *IEEE Trans. Automat. Control*, **38**(1), 58–69.
- Suresh, S. (1991). *Fatigue of Materials*. Cambridge University Press, Cambridge, U.K.
- Tangirala, S., A. Ray and M. Carpino (1995). Damage-mitigating control of mechanical structures: experimental verification of the concept. *Smart Mater. Struct.* **4**(2), 139–146.
- Tangirala, S. (1996). Stochastic modeling of fatigue damage for on-line monitoring, prognostics and life-extending control. Ph.D. Dissertation, Mechanical Engineering Department, Pennsylvania State University, May.
- Vidyasagar, M. (1992). *Nonlinear Systems Analysis*, 2nd ed. Prentice-Hall, Englewood Cliffs, NJ.